



In situ and real-time ultrafast spectroscopy of photoinduced reactions in perovskite nanomaterials

Received: 8 February 2024

Accepted: 20 May 2025

Published online: 28 May 2025

Check for updates

Gi Rim Han¹, Mai Ngoc An^{1,4}, Hyunmin Jang^{1,2}, Noh Soo Han^{1,5}, JunWoo Kim^{1,6}, Kwang Seob Jeong^{1,2}, Tai Hyun Yoon^{1,3}✉ & Minhaeng Cho^{1,2}✉

By employing two synchronized mode-locked femtosecond lasers and interferometric detection of the pump-probe spectra—referred to as asynchronous and interferometric transient absorption—we have developed a method for broad dynamic range and rapid data acquisition. Using asynchronous and interferometric transient absorption, we examined photochemical changes during femtosecond pump-probe experiments on all-inorganic cesium lead halide nanomaterials. The laser pulse train facilitates photoreactions while allowing real-time observation of charge carrier dynamics. In perovskite nanocrystals undergoing photo-substitution of halide anions, transient absorption spectra showed increasing bandgap energy and faster relaxation dynamics as the Cl/Br ratio increased. For colloidal perovskite nanoplatelets, continuous observation revealed both spectral and kinetic changes during the light-induced coalescence of nanoplatelets, by analyzing temporal segments. This integrated technique not only deepens understanding of exciton dynamics and environmental influences in perovskite nanomaterials but also establishes asynchronous and interferometric transient absorption as a transformative tool for real-time observation of photochemical dynamics.

In spectroscopy, researchers frequently encounter a dilemma when the tool they employ for observation—light—also triggers alterations in their target materials and molecular systems. This problem is particularly pronounced for ultrafast spectroscopy methods. Here, prolonged exposure to high-energy laser light is imperative to capture subtle and weak nonlinear responses. The situation underscores the challenge: the acquisition of data under such circumstances becomes demanding and, at times, seemingly impossible. Therefore, the reduction of data acquisition (DAQ) time is essential when the observed materials deviate from established photostability standards.

The efficacy of asynchronous optical sampling in curtailing DAQ time is well-established, as it eliminates the need for linear stages to generate time delays between pump and probe pulses^{1,2}. Although

initially proposed and demonstrated nearly half a century ago, our group has been in pursuit of advancing this technique across various bandwidth ranges and has applied it to a wide array of biological and material systems^{3–6}. However, the broader research community in ultrafast spectroscopy remains incompletely cognizant of its utility for rapid and stable transient absorption and multidimensional spectroscopic measurements. In this work, we introduce and apply our novel spectroscopic approach, asynchronous and interferometric transient absorption (AI-TA)⁷, to investigate the photochemical reactions of perovskite nanocrystals (PeNCs) and nanoplatelets (PeNPLs).

Perovskite nanomaterials have attracted considerable attention for their applications, such as light-emitting diodes⁸ and single-photon sources in quantum technologies⁹. Despite their susceptibility to form

¹Center for Molecular Spectroscopy and Dynamics, Institute for Basic Science, Seoul, Republic of Korea. ²Department of Chemistry, Korea University, Seoul, Republic of Korea. ³Department of Physics, Korea University, Seoul, Republic of Korea. ⁴Present address: Quantum Science Ltd., Warrington, UK.

⁵Present address: Korea Research Institute of Standards and Science, Daejeon, Republic of Korea. ⁶Present address: Department of Chemistry, Chungbuk National University, Cheongju, Republic of Korea. ✉e-mail: thyoona@korea.ac.kr; mcho@korea.ac.kr

trap and defect states due to a high surface-to-volume ratio in colloidal dispersions^{10,11}, these materials exhibit advantageous properties, including high defect tolerance¹², tunable bandgap levels¹³, and a simple, cost-effective synthesis process¹⁴. Additionally, they possess notable physical attributes such as high quantum yields^{15,16} and enhanced stability¹⁷, making them promising candidates for photovoltaic and optoelectronic devices.

Given their potential applications in solar cells and light-emitting devices, the interaction of perovskites with light has become a subject of significant interest among researchers and engineers. Beyond time-resolved studies of carrier and quasiparticle dynamics, perovskite nanomaterials display a range of light-induced behaviors, including degradation, which has emerged as a key focus in recent research. Here, utilizing the rapid DAQ capabilities of AI-TA, we simultaneously investigate both ultrafast carrier dynamics via femtosecond pump-probe measurements and light-induced transformations in perovskite nanomaterials, where two distinct types of photoreactions are considered.

The first study examines photoinduced halide substitution of PeNCs. A key feature of PeNCs is their possibility of post-synthesis compositional modification through the use of appropriate salts containing halide anions, as they can freely diffuse into and out of the rigid cation lattice¹⁸. The halide composition significantly influences the bandgap energy, allowing the emission wavelength to be tuned across the visible spectrum. For instance, iodide-based PeNCs exhibit red to near-infrared emission, while bromide and chloride shift the bandgap toward blue and near-ultraviolet regions¹³.

Recent studies have reported halide anion substitution in perovskites through a photoinduced process^{19,20}. This phenomenon can take place when PeNCs are dissolved in halide-containing solvents (e.g., chloroform and dibromomethane) and concomitantly exposed to light. The proposed mechanism involves the dissociation of solvent molecules upon interaction with photoexcited PeNCs, facilitated by interfacial electron transfer^{19,21}. The high reduction potential of these solvents relative to PeNCs enables photoinduced electron transfer, extracting halide anions from the solvents. These anions can then exchange and diffuse within the PeNC lattice. The photoinduced anion-exchange process allows remote control over the extent and composition of substitution²⁰ while preserving the size and morphology of the nanoparticles²². Additionally, it has been shown to mitigate vacancy defects, enhance crystallinity²³, and facilitate cation exchanges as well²⁴, further broadening the potential applications of PeNCs.

The second system under investigation involves photon-driven transformations of PeNPLs. PeNPLs represent a distinct class of nanomaterials with unique morphology and physical properties compared to PeNCs. Their defining characteristic arises from confinement along a single-dimensional axis, with thinner platelets exhibiting higher bandgap energy²⁵. However, their colloidal stability in solution is limited, and PeNPLs are known to aggregate into higher-order structures, including bulk-like status when exposed to heat^{26,27}, light^{28–31}, polar solvents³², or prolonged ambient conditions³³. Particularly, this phenomenon occurring under light exposure is referred to as photon-driven transformation.

Such behavior is not exclusive to PeNPLs and can also occur in other colloidal forms, including PeNCs and perovskite nanorods³⁴. However, PeNPLs are especially prone to aggregation into higher-dimensional structures. This process often begins with pre-assembly into self-assembled superlattices, where discrete nanoplatelets stack with ligands spacing the ionic crystal layers³⁴. These intermediate assemblies may aggregate into larger structures, sometimes forming mosaic-like superstructures^{26,27}. In this second study, the AI-TA technique is applied to track real-time changes occurring in PeNPLs during the pump-probe measurement, without the deliberate introduction of reactants as in the previous case. Time-resolved in situ observations reveal coalescence-induced changes in the transient absorption

spectra of PeNPLs, demonstrating the technique's capability for monitoring light-induced dynamic transformations of perovskite nanomaterials.

In this Communication, we begin by providing an overview of our approach, AI-TA, emphasizing how its capabilities enable the distinct observations presented in this study. We then analyze the transient dynamics and spectral features of PeNCs dispersed in toluene solvent under non-reactive conditions. Subsequently, we explore the in situ photoinduced substitution process, examining changes in the bromide-to-chloride ratio and their effects on the ultrafast transient absorption spectra of charge carriers. For the next target, we investigate PeNPL colloidal dispersions using AI-TA, tracking spectral and temporal changes as the nanoplatelets aggregate into higher-order structures. In addition to presenting novel photophysical insights from these two experiments, we demonstrate that AI-TA is a powerful technique for rapid DAQ, enabling in situ ultrafast spectroscopy to monitor processes occurring over extended timescales.

Results and discussion

Asynchronous and interferometric transient absorption (AI-TA) spectroscopy

Numerous attempts have been made to reduce the DAQ time associated with transient absorption, one of the most widely used third-order nonlinear spectroscopy techniques. Reflecting on past initiatives, such as the adoption of array detectors and computational data reconstruction, we can identify two key rate-determining factors^{1,35,36}: first, the generation of pump-probe time delays using linear stages, and second, the execution of data averaging to reduce noise levels.

AI-TA overcomes the limitations imposed by conventional techniques by eliminating the need for a linear stage to generate pump-probe delays. Instead, it employs a pair of repetition rate-stabilized mode-locked lasers. When the two lasers have slightly different repetition rates, they generate time steps proportional to the difference in repetition rates (Fig. 1a), referred to as the detuning frequency (Δf). This method ensures consistent spatial overlap of the pump and probe beams, regardless of the duration of the time delays. The equation below shows how to calculate each time step (Δt) generated by a pair of pump and probe pulses with repetition rates, f_r and $f_r + \Delta f$, respectively:

$$\Delta t = \frac{1}{f_r} - \frac{1}{f_r + \Delta f} = \frac{\Delta f}{f_r(f_r + \Delta f)} \approx \frac{\Delta f}{f_r^2} = \frac{f_D}{f_r} \quad (1)$$

The approximation in Eq. (1) is valid due to the significantly small detuning frequency Δf compared to the repetition frequency (f_r), i.e., $\Delta f \ll f_r$. An important point to note is that the down-conversion factor $f_D = \Delta f / f_r$ can be precisely controlled by a GPS-disciplined Rb atomic clock, ensuring consistent generation of time steps^{37,38}. Additionally, when the separated pump and probe pulses overlap in space and time on another BBO nonlinear crystal for sum-frequency generation, distinct trigger signals are produced at a rate of $1/\Delta f$, marking the initiation of the pump-induced probe response.

In conventional transient absorption techniques, obtaining wavelength-resolved information in the time domain requires a monochromator or spectrograph equipped with a charge-coupled device. In our approach, we accomplish this by generating a self-referenced interferogram (see Supplementary Fig. 1 for the pump and probe spectra). The position of the linear stage corresponds to the time delay between split probe pulses, so scanning the stage at a constant velocity produces an autocorrelation signal (Supplementary Fig. 2). Using frequency domain detection with a single point detector offers advantages in terms of effective noise filtration and signal collection efficiency.

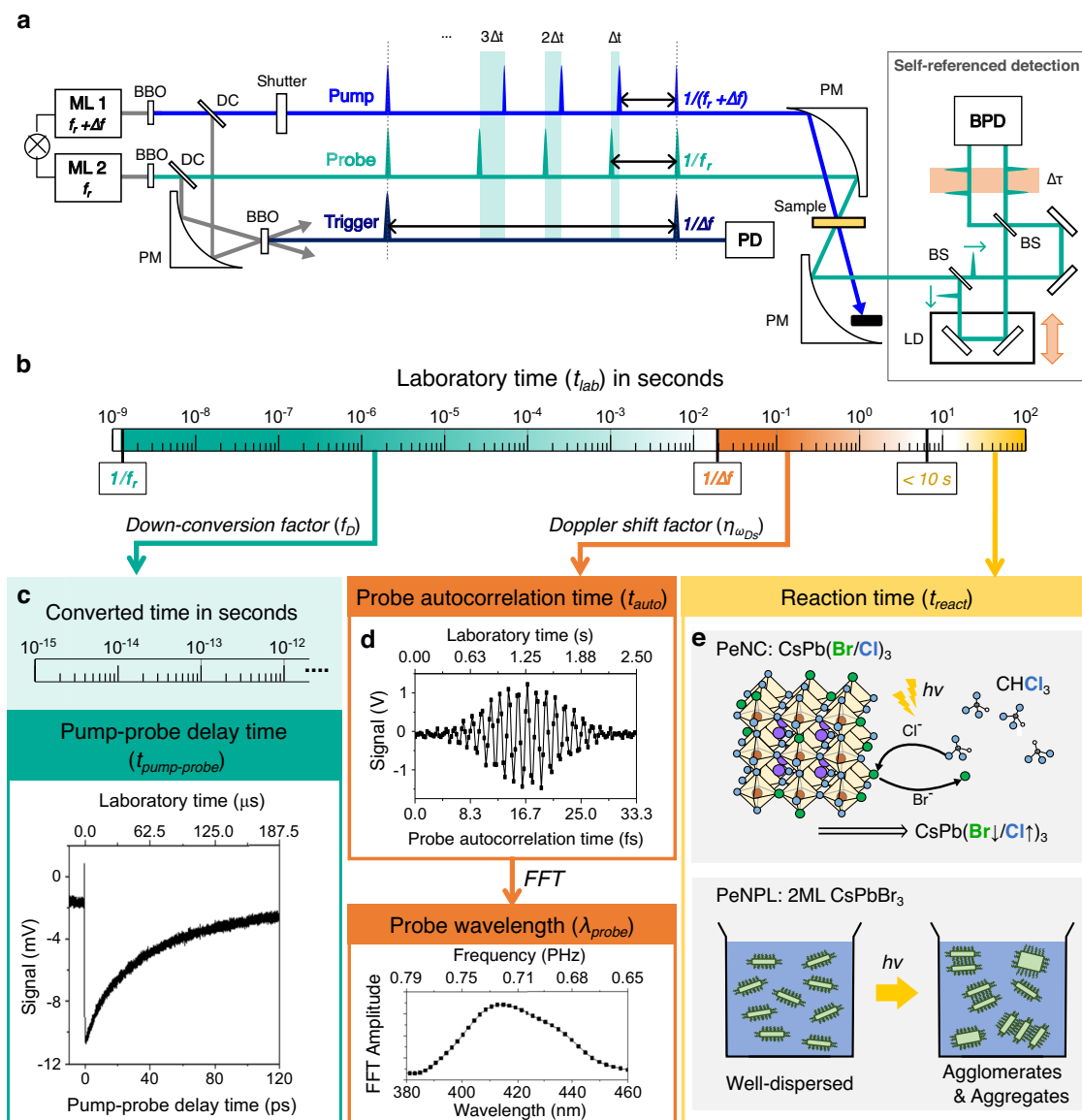


Fig. 1 | Schematics of AI-TA instrumentation and parameters. **a** Experimental setup of the AI-TA. The spectra of ML1 and ML2 are shown in Supplementary Fig. 1. ML mode-locked laser, DC dichroic mirror, BBO beta barium-borate crystal, PD photodiode, BS beam-splitter, PM parabolic mirror, BPD balanced photodiode, LD linear delay stage. The self-referenced interferogram is acquired through a Mach-Zehnder configuration and detected using a balanced photodetector. **b** Definition of the time variables in relation to the laboratory time, t_{lab} . By using time-division multiplexing, the laboratory time can be processed into pump-probe delay time ($t_{pump-probe}$), probe autocorrelation time (t_{auto}), and reaction time (t_{react}). **c** An example of a transient signal depending on the $t_{pump-probe}$, which is converted from the laboratory time using the down-conversion factor, f_D . Here, when

$f_r = 80.0$ MHz and $\Delta f = 51.2$ Hz, $187.5 \mu\text{s}$ of laboratory time is required to complete a single scan of pump-probe delay from 0 to 120 ps. **d** The interferogram was acquired by collecting signals sampled at the rate of $\Delta f = 51.2$ Hz, while the linear delay stage is moving at a constant velocity of $2 \mu\text{m/s}$. The laboratory time in this case can be converted to the t_{auto} using the Doppler shift factor $\eta_{\omega_{Ds}}$. Fast Fourier transform of the data yields the probe spectrum with respect to the wavelength, λ_{probe} . **e** Experimental schematic of the ultrafast pump-probe investigation of photoinduced reactions of perovskite nanomaterials. Since the pump and the probe lights work as reaction stimulants that induce photo-substitution or photon-driven transformation, the data acquisition measurement time can be considered as t_{react} .

In our setup, the probe intensity is detected by a fast digitizer operating at a sampling rate of f_r , synchronized with the repetition rate of the probe laser. The probe signal contains information about both the linear absorbance of the sample and its pump-induced non-linear responses. Since the raw data consists of an array of voltage signals that are time-tagged by optical trigger signals, time-division multiplexing can be applied to acquire information from segments of different temporal lengths^{3,38}. In Fig. 1b, to avoid confusion in the upcoming discussions, we define four temporal variables involved in the interpretation of AI-TA data. The time tag from the digitizer represents the real-world time measured during the experiment, also referred to as laboratory time (t_{lab}). Given that our system records data

every 12.5 ns, the temporal span over a 1-h experiment encompasses eleven orders of temporal dynamic range. This extensive time span allows the analysis of additional time-dependent variables that influence the probe response if they operate in temporally distinct regimes. Based on this, laboratory time is divided into three segments in this study: pump-probe delay time, probe autocorrelation time, and reaction time.

First and foremost, using the relationship (Eq. 1), we can convert the laboratory time, recorded at an interval of $1/f_r$, to the pump-probe delay time ($t_{pump-probe}$) by multiplying it with the down-conversion factor f_D . In Fig. 1c, the pump-probe response of the PeNC solution is shown as a function of $t_{pump-probe}$. The starting time, or time zero, of

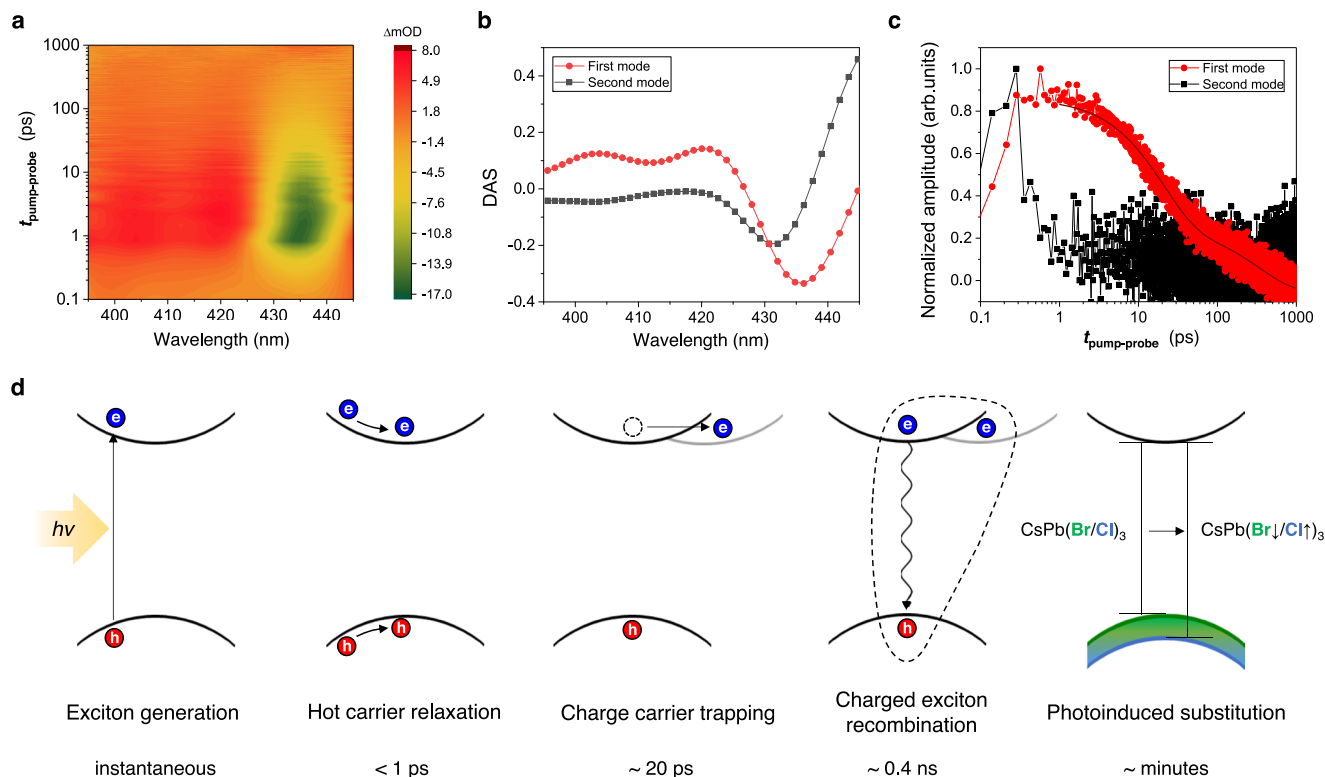


Fig. 2 | Photodynamics of PeNCs. **a** The transient absorption spectrum of CsPb(Br/Cl)₃ PeNCs dissolved in toluene measured up to 1 ns. The spectrum is the averaged result of 200 scans. **b** Decay-associated spectra and **c** time-resolved decay profiles of the first two modes from singular value decomposition analysis. The second mode decays quickly within 1 ps, and the first mode persists over a longer period, which has been analyzed with a bi-exponential fit. **d** List of various dynamics observable with the AI-TA technique spanning a broad dynamic range from subpicosecond to minutes. The initial pump pulse instantaneously generates holes and

electrons. As the excitation energy exceeds the bandgap energy, any excess energy is quickly dissipated as the hot carriers relax to the band-edge state. This transition is accompanied by bandgap renormalization. Due to the presence of trap states near the band edge, the conduction band is partially depopulated with a short lifetime of ~20 ps. The shallow nature of this charge trap allows interaction with other excitons, resulting in a charged exciton recombination with a lifetime of 0.35 ns. During the experiment photoinduced halide substitution occurs with timescales of minutes.

the signal is defined by the optical trigger signal. Then, the pump-induced transmission change is calculated by dividing the voltage signals recorded after the trigger by those recorded before the trigger.

The interferogram generated by scanning the linear stage contains information about the frequency of the electromagnetic field, which can be easily accessed through a fast Fourier transform (FFT). The method requires the data points of the interferogram to be evenly spaced in time. Provided that the linear stage moves at a fixed velocity, this can be achieved by using the trigger rate, Δf , as the sampling frequency, as shown in Fig. 1d. The time interval between each sample ($\Delta\tau$) can be calculated using the Doppler shift relation $\omega_{\text{Ds}} = 2\omega v/c$, where ω is the angular frequency of the probe field, v is the stage speed, and c denotes the speed of light. Then, we can deduce that $\Delta\tau = 2v/c\Delta f = \eta_{\omega_{\text{Ds}}}/\Delta f$. The Doppler shift factor, $\eta_{\omega_{\text{Ds}}} = 2v/c$, is multiplied by t_{lab} to calculate the effective time between split probe pulses, known as the probe autocorrelation time (t_{auto}).

From here, we can extract frequency-resolved light intensity via FFT, which can also be expressed in terms of probe wavelength (λ_{probe}) using the speed of light c . Since each data point is annotated with a corresponding t_{lab} in relation to trigger time zero, our approach allows simultaneous measurement of decay lifetimes for each spectral component, provided the linear stage scanning speed is significantly slower than the rate of pump-probe delay generation time $t_{\text{pump-probe}}$. More detailed and advanced theoretical descriptions and comprehensive analyses of experimental parameters related to this technique have been presented and demonstrated in our previous works^{3,7,39}. Our implementation, AI-TA, also features a high duty cycle and low energy

per pulse, rendering it particularly advantageous for scenarios involving photoreactions and photodamage.

Figure 1e presents two target systems for the ultrafast pump-probe investigation in this study and defines the final time parameter, i.e., reaction time (t_{react}). This experimental design is conceived to integrate both synthesis and analysis, with the pump and probe lights serving as both reaction stimulants and observation tools simultaneously. Meanwhile, the rapid DAQ procedure of our AI-TA setup enables data collection before significant changes occur in the perovskite nanomaterials. Since the data from each linear stage scan are saved as discrete files with corresponding timestamps, we can determine the interval between subsequent measurements, which is less than 10 s (Supplementary Fig. 3). Thus, this measurement time can be considered as the reaction time in our analysis. Note that t_{react} has fewer significant digits, as it is not governed by the precision of an atomic clock.

AI-TA measurement of CsPb(Br/Cl)₃ in toluene

Before proceeding to in situ analysis, we first analyzed the transient absorption spectrum of the nanocrystals dissolved in toluene to investigate the dynamics involved in the relaxation of PeNCs. Since this solvent does not contain halide agents, halide exchange is avoided. The resulting TA spectrum, shown in Fig. 2a, represents an average of 200 interferogram scans. We applied singular value decomposition (SVD) and selected the first two eigenmodes as the principal representations of the states contributing to the overall transient absorption signal (Supplementary Fig. 4).

The decay-associated spectrum (DAS) of the first mode exhibits a strong negative optical density near 435 nm, indicative of a bandgap photo-bleaching (PB) signal, with a possible contribution from stimulated emission (Fig. 2b). Additionally, distinctive peaks of excited-state absorption (ESA) appear below 425 nm, resulting from the quantum confinement effect in our PeNCs^{40–42} (Supplementary Fig. 5).

A bi-exponential fit to the time profile of the first mode yields two lifetimes: 20.2 and 345.5 ps (Fig. 2c). The shorter component, decaying within tens of picoseconds, is typically associated with biexciton decay or the Auger recombination process^{40,43–46}. However, given our exceptionally low pump energy of 0.5 nJ per pulse, this is better described by the charge carrier trapping process originating from shallow defects on the surface^{47–49}. The intrinsically low power of our spectroscopic apparatus allows us to bypass the consideration of multi-exciton formation, which can occur when using high-power pumps and requires many-body analyses to extract one-exciton dynamics from the complicated TA signals⁵⁰.

On the other hand, lifetimes on the order of hundreds of picoseconds are primarily associated with trap-mediated decay or recombination of charged excitons, known as trions^{44,46}. It is important to note that the decay of unaffected excitons typically occurs on the order of a few nanoseconds^{40,44}. The decay of charged excitons is observed even under low fluence, as their formation is closely tied to charge traps in surface defects^{51,52}. Both observations are consistent with the high trap density of chloride-based perovskite nanomaterials, which creates a significant barrier to their application as blue light emitters⁵¹.

For the second mode, its time profile decays within one ps. Such a sub-picosecond transition is often a complex signal and difficult to identify due to the concurrent contributions of coherent artifacts, such as scattering signals, within this temporal range⁵³. The DAS of the second mode shows a negative peak at an energy level higher than the PB peak of the first mode, which is a characteristic of hot carrier thermalization and relaxation^{45,54}. The pronounced ESA feature observed here is linked to the bandgap renormalization process^{41,43}. Thus, we interpret the second mode as indicative of the initial excited state undergoing intra-band relaxation.

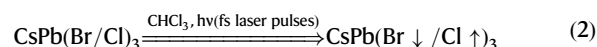
An overview of the discernible kinetics achieved through our technique is presented in Fig. 2d based on distinct lifetimes and spectral features. The shorter PB decay originates from the emptying of the conduction band-edge to shallow traps, while the longer PB decay is induced by the recombination of charge carriers to the ground state. The radiative decay lifetime is confirmed through time-resolved fluorescence measurements (Supplementary Fig. 6).

Our unique contribution to the study of photodynamics is shown in the final panel of Fig. 2d, which will be discussed in the following sections. This portion illustrates the photoinduced substitution of the halide composition of PeNCs, occurring over an extended duration, spanning minutes. The figure is based on reports suggesting that the impact of halide composition primarily affects the valence band, driven by the interaction between hot phonons and holes⁵⁵. Our AI-TA technique enables the observation and analysis of the distinct physical properties exhibited by each composition generated through light exposure.

Photoinduced halide substitution of CsPbX₃ nanocrystal

The first subject of our study involves PeNCs with a mixed halide composition, specifically CsPb(Br/Cl)₃, dissolved in a chloroform/toluene mixture. Upon irradiation, the bromide ions in the PeNCs are substituted with chloride ions. As described earlier, this anion-exchange reaction occurs as a result of the photoinduced electron transfer process, in which the PeNCs extract halides from the surrounding solvents, leading to the formation of a new composition. The overall process can now be summarized by the following

photochemical equation:



where PeNC, denoted as CsPb(Br ↓ / Cl ↑)₃, differs from CsPb(Br/Cl)₃ due to the substitution of Br with Cl.

Since the equilibrium between the nanocrystals and the solvated halide anions is reached almost instantly, within a few seconds¹⁸, continuous DAQ under these conditions allows for in situ observation of the transforming PeNCs. The high-speed DAQ enabled by AI-TA significantly mitigates the influence of the pump and probe on the system during each scan. Remember that each interferogram scan, including the data-saving process, takes less than 10 s, which is a substantial improvement over conventional techniques. However, due to inherent noise in the data from a single interferogram, averaging is necessary (Supplementary Figs. 7 and 8). The transient mapping shown afterward represents an average of a few scans, culminating in an approximate acquisition time of 1 min, which is required to delineate the transient features.

Figure 3a shows the absorption and emission spectra of PeNC in toluene/chloroform, before and after 20 min of AI-TA experimentation, and Fig. 3b depicts the spectral evolution of transient absorption spectra, reflecting the first and the last minute of the experiment. Both the absorption edge and the PB peak initially appeared around 440 nm but shifted to 430 nm, indicating a change in bandgap energy levels. The PB peak positions closely match the steady-state absorption and emission spectra measured before and after the experiment, as shown in the top panel of the figure. This measurement result provides evidence of a shifting bandgap while upholding the confined nature of the system.

To verify compositional changes, the remaining stock solution and the solution collected after the AI-TA experiment were analyzed using other materials analysis methods. X-ray photoelectron spectroscopy (XPS) analysis, shown in Fig. 3c (wide scan in Supplementary Fig. 9), corroborates the compositional changes in the PeNCs before and after a separate 30-min AI-TA experiment (Supplementary Fig. 10). The peaks corresponding to the elements are magnified in the panel to highlight the compositional changes. The Cl/Br ratio shifts from 1.72:1.28 to 2.24:0.76 in the pre- and post-photo-substituted samples, respectively. Additionally, the size of the nanocrystals remains unchanged, suggesting that the observed shift in bandgap is not due to changes in the nanocrystal dimensions (Fig. 3d). The average sizes are 7.1 (±1.1) nm and 7.2 (±1.1) nm for the samples before and after photoinduced anion-exchange reaction, respectively. The results confirm that halide exchange occurred while preserving most of the macroscopic physical properties, although some physical degradation may have also occurred (Supplementary Fig. 11).

Analysis of the parameters involved in halide substitution

Before conducting an in-depth analysis of the AI-TA data scans, it is imperative to verify the orthogonality of the time parameters. The independence of these parameters is confirmed by monitoring the PB peak throughout the experiment, as depicted in Fig. 4a. The peak position of each successive data point falls within the error bars of both the preceding and following measurements, which validates the orthogonality between each transient absorption spectra map and the reaction time t_{react} . It is important to note that the reaction reaches completion after ~100 min, indicating a dynamic equilibrium between the halides in the PeNCs and those dissolved in the solvent. The photoreaction can also be characterized by an approximate lifetime of 46 min, as determined by fitting the peak position (Supplementary Fig. 12).

The effects of the halide solvent and irradiation are validated through multiple control experiments. When toluene is used as the

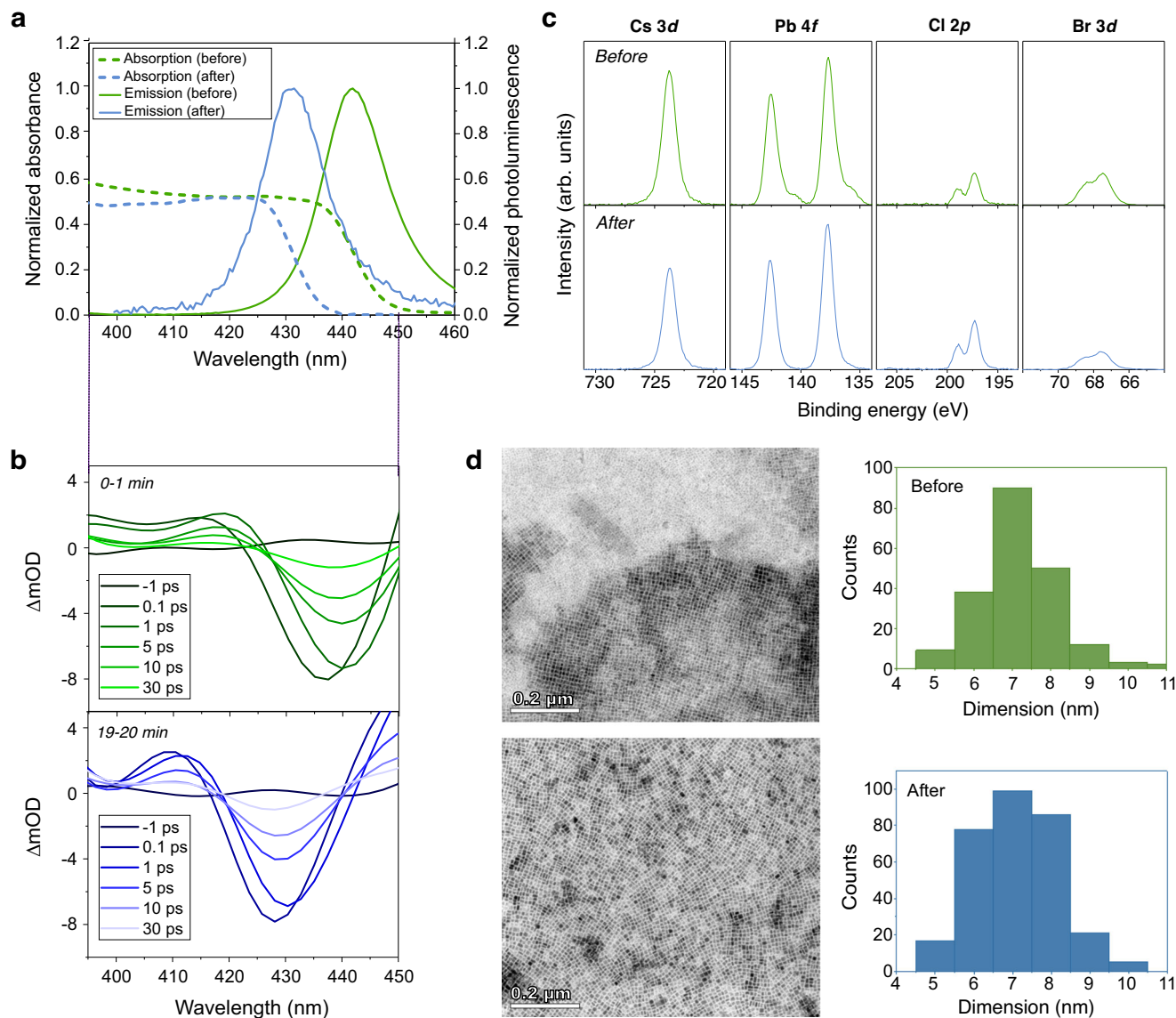


Fig. 3 | Photo-substitution of PeNCs. **a** Comparison of absorption and emission spectra acquired before and after the AI-TA experiment of PeNC in chloroform. **b** Transient absorption of the first- and the last-minute scan of the experiment showing spectral evolution. The blueshift of the PB peak and corresponding steady-state spectra confirm the increased bandgap of the nanocrystal. **c** X-ray

photoelectron spectroscopy (XPS) results for the PeNC sample before and after an AI-TA experiment of PeNC in chloroform. **d** TEM image of PeNCs measured before and after the AI-TA experiment of PeNC in chloroform, and the histogram showing size distribution. The scale bar of the image is 0.2 μm .

sole solvent, the peak position remains unchanged throughout the experiment (Fig. 4b). However, when chloroform is introduced to the solvent, the PB peaks exhibit a blueshift, highlighting the effect of solvent composition on the rate of photo-substitution within the PeNCs. The rate and final halide ratio of photoinduced exchange have been reported to depend on the ratio of toluene to halide solvents²³. Additionally, the concentration of PeNCs, and consequently their optical density, is shown to influence the kinetic rates (Supplementary Fig. 13a). The critical role of halide solvents is further demonstrated by the reverse substitution from chloride to bromide when dibromomethane is used as the halide solvent instead of chloroform (Supplementary Fig. 13b).

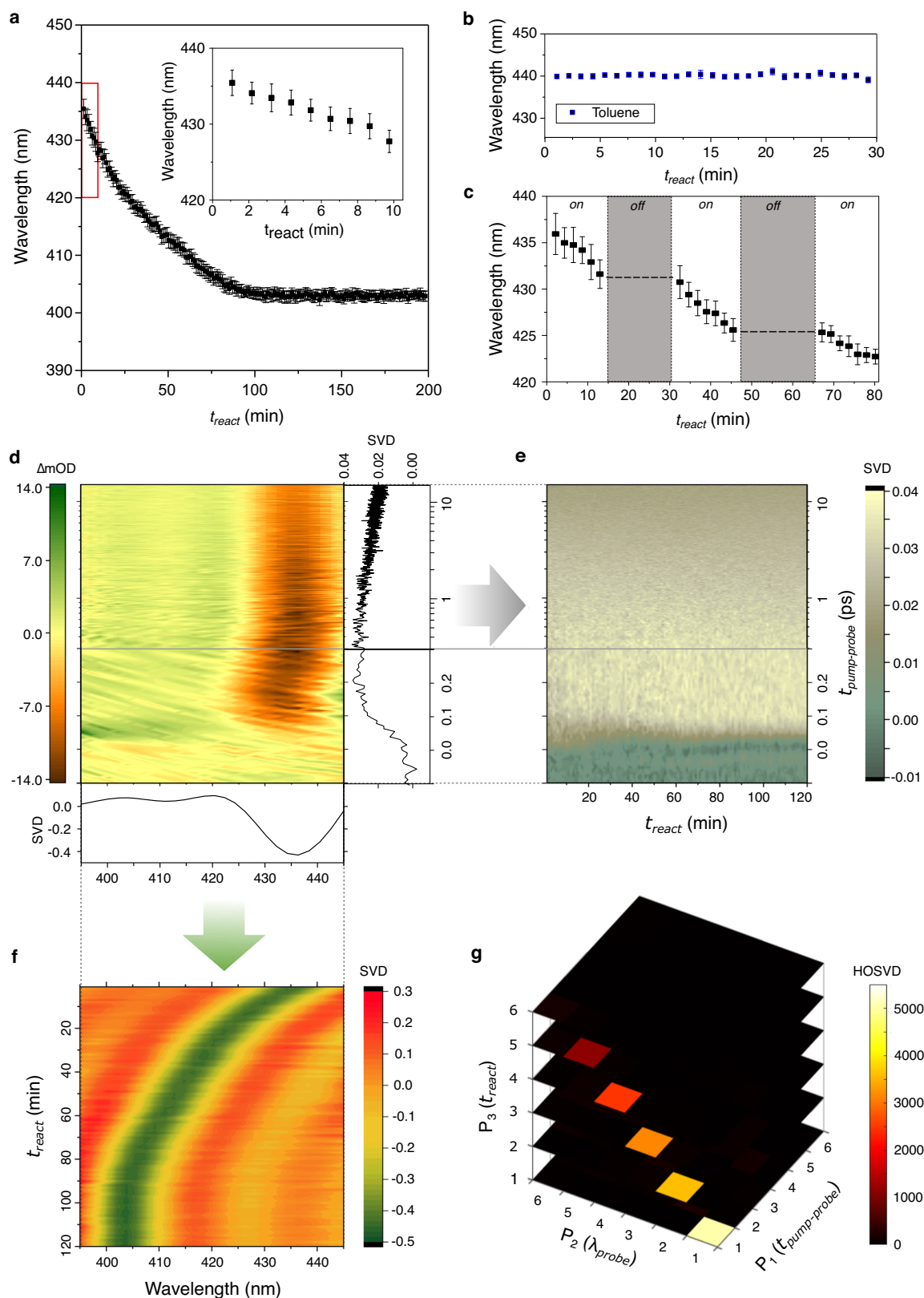
The role of light as a reaction trigger is confirmed through a temporary pause in measurements (Fig. 4c). While the peak position shifts during continuous irradiation, it remains unchanged in the absence of light. The observations corroborate both halide solvents

and irradiation as key factors in the photoconversion process between halides in PeNCs and those bound to the solvent.

Furthermore, the use of a high-repetition-rate oscillator may induce heating in addition to irradiation for photoinduced chemical reactions. To assess the potential contribution of this effect to the substitution process, we conducted a control experiment by heating a PeNC/chloroform solution in the dark. The steady-state spectra (Supplementary Fig. 13c) remained unchanged, indicating that thermal effects are negligible.

Figure 4d presents processed data from the initial data segment, which is the averaged result of 10 interferogram scans and corresponds to less than 1 min of t_{react} , where the nonlinear response is plotted with respect to $t_{\text{pump-probe}}$ and λ_{probe} . This yields information typically acquired from conventional transient absorption.

The inclusion of the t_{react} axis emphasizes the advantage of our approach over conventional methods, as it enables the identification



of variations in spectral or temporal signatures that depend on t_{react} , which in this case is associated with photo-substitution. Figure 4e presents the decay profiles of the first mode, obtained from the SVD of data averaged over every ten scans, illustrating the relationship between $t_{\text{pump-probe}}$ and t_{react} . The plot clearly shows that the ultrafast rise of the PB signal, identified earlier as hot carrier relaxation,

becomes shorter as reaction time progresses. The thermalization of hot carriers is known to depend on the excess energy provided by the pump above the bandgap⁵⁴. Since our pump energy and fluence remain constant throughout the experiment, the observed behavior of the rise signal can be attributed to the bandgap energy increasing until it aligns with the pump range. It is important to note that this trend

Fig. 4 | Comprehensive mapping of AI-TA analysis results. **a** Extended PB peak tracking over 3 h of the experiment. The inset zooms in to show that each sequential peak lies within the error bar of the prior measurement. **b** Tracking PB peaks of PeNCs in toluene over the course of the experiment, showing that halide solvent is required for the peak shift. **c** Effect of light on PB peak. Peak positions shift when a measurement is ongoing but remain the same when the experiment is paused, signaling that the shift is a light-induced process. The error bars in (a–c) are obtained by calculating the standard deviation of PB peak wavelengths collected from the $t_{\text{pump-probe}}$ delay within 1 to 5 ps. **d** Analysis of the initial 1-min data acquired from AI-TA measurement. The trend along $t_{\text{pump-probe}}$ axis provides insight into the kinetic parameters and lifetime of the photophysical processes of PeNCs,

while the λ_{probe} -dependent spectrum provides spectral information of excited states. Along each axis, the first mode acquired from singular value decomposition is plotted. **e** Decay profiles of the first mode acquired from SVD of data decomposed into 1-min intervals of t_{react} , showing its relationship with $t_{\text{pump-probe}}$. **f** $\lambda_{\text{probe}}-t_{\text{react}}$ correlation map showing the evolution of spectral characteristics with the duration of the experiment. **g** Reduced core tensor for extended 2-hours-long measurement, which is the result of the high-order singular value decomposition (HOSVD) analysis of the AI-TA experiment data. Here, the index of each axis represents singular values arranged in descending order from the highest to the lowest, which are truncated to show only major modes involved in the dynamics.

appears to plateau near 60 min, well before the PB peak shift halts. The early cessation of the change in thermalization rate may be due to the bandgap entering the pump spectrum range (Supplementary Fig. 1).

From these results, we can infer that having excess energy results in a longer thermalization and bandgap renormalization process in the sub-picosecond decay. Also, the exponential fitting of PB decay shows a slight decrease in lifetime as chloride photo-substitution progresses (Supplementary Fig. 14). Given that we have linked this parameter to the charge trapping of electrons in shallow traps, this relationship suggests that higher chloride content accelerates charge trapping. Interestingly, similar observations have been reported, where a faster charge-induced trapping rate was correlated with higher chloride content in PeNCs⁴⁷. Since vacancies are more abundant in higher chloride compositions, the increased trap density facilitates better separation of charge carriers such as electrons. Moreover, because PeNCs are continually exchanging ions with surrounding solvent molecules, the high variability in trap density and consequently the lifetimes can also be explained.

In Fig. 4f, a similar analysis of the DAS of the first mode against t_{react} shows that spectral characteristics are evidently influenced by the duration of the experiment. This $\lambda_{\text{probe}}-t_{\text{react}}$ correlation map reveals a blueshift in the PB peak, reaching 403 nm, consistent with the peak analysis shown in Fig. 4a. From the evidence presented so far, we can confidently assert that the real-time evolution of spectral characteristics is a result of the substitution of bromide with chloride. Overall, this illustrates the multidimensional nature of a single AI-TA measurement under photo-responsive conditions, a capability made possible by our technique.

Building upon this, we can parameterize three orthogonal variables based on the temporal order of the time segments defined earlier. First, P_1 represents the transient time-resolved response after the incidence of the pump pulse, which is related to $t_{\text{pump-probe}}$. P_2 corresponds to bandgap energy-resolved information of PeNCs in terms of λ_{probe} , obtained from the FFT of the interferogram scan. Lastly, P_3 reflects the halide ratio of PeNCs, based on the unidirectional photo-substitution from bromide to chloride, and is associated with the total DAQ time divided into 1-min intervals, corresponding to t_{react} . By examining the dynamic responses between any pair of these parameters, we can identify correlations within the system. Since the raw data arrays can be structured as a rank-three tensor using three-fold time-division multiplexing, we can isolate states or modes related to a single parameter of P_n ($n=1, 2, 3$) and establish the relationships between these states through tensor decomposition analysis. In other words, the decomposed tensors can be projected into corresponding 2-dimensional planes.

To demonstrate and simplify the picture of parameter correlations, we apply higher-order SVD (HOSVD) to 2-h-long experimental results^{56,57}. The truncated core tensor, or decomposed projection, of this analysis is portrayed in Fig. 4g (Supplementary Table S1). The visualization summarizes and highlights the relationships discussed earlier. The prominent diagonal values along the P_2-P_3 basis correspond to the progression of different wavelength modes along the t_{react} axis. In other words, it shows the shift in bandgap energy as the

chloride composition increases and the bromide composition decreases. Conversely, the distinctly lower values, apart from the first mode of the P_1 basis, indicate that a single decay profile dominates, regardless of λ_{probe} or t_{react} .

Through an iterative fabrication approach, often referred to as compositional engineering, remarkable strides have been achieved in developing efficient perovskite solar cells^{58–61} and light-emitting devices⁶². This concept also extends to the quantum yield efficiency of PeNCs⁵⁵. The importance of halide composition has been emphasized in studies highlighting the close link between the purity of a single-photon source and its halide composition⁶³. Halide exchange, usually induced by salt-based mechanisms, has been a topic of great interest for those who study the effects of compositional modifications while preserving morphology and minimizing other structural influences^{43,47,54,64}. In particular, chloride substitution, despite its favorable bandgap for blue or ultraviolet light sources, has faced challenges in practical applications due to low quantum yield and relatively poor power conversion efficiency^{51,65}. Although compositional engineering has proven to be effective, it remains a time-consuming and complex process. As a result, considerable efforts have been directed toward evaluating photoluminescence lifetimes through in-line synthesis⁶⁶. Our strategy, utilizing AI-TA, offers a faster and more precise method for halide composition engineering.

AI-TA measurement of photon-driven transformation process

In the next phase of our AI-TA investigation, we observed changes in the transient features of PeNPLs dispersed in hexane as the measurement progressed. PeNPLs are characterized by stronger exciton binding energy due to enhanced quantum confinement from thickness control. The thickness is quantified by the number of lead halide octahedra layers, referred to as monolayers (MLs), in the quantum-confined dimension. In addition to varying the halide composition mentioned earlier, the bandgap energy of PeNPLs can also be tuned by controlling the confinement thickness. This approach is effective for only a few MLs, as the effective Bohr radius for exciton in CsPbBr₃ is ~7 nm, and the size of a cubic unit cell is 0.58 nm^{13,31,67}.

The composition investigated here consists of cesium lead bromide with a 2 ML confinement layer. This is the thinnest variant, other than 1 ML, which consists of a single layer of lead halide octahedra without cesium cations and is stabilized with ligands. A TEM image confirms the formation of PeNPLs with an approximate size of 20 nm in the non-confined dimension (Fig. 5a), which is known not to affect the peak energy significantly⁶⁸. The absorption and emission spectra of the synthesized CsPbBr₃ PeNPLs show peaks near 430 nm, consistent with reported values, whereas bulk materials with the same composition show peaks near 530 nm^{68,69}. The sharp excitonic peak confirms the large binding energy that is characteristic of PeNPLs. After the AI-TA measurement, the steady-state spectra reveal the appearance of additional peaks in the longer wavelength region (Fig. 5b). The red-shifted spectrum matches the characteristic multiple peaks of higher-order PeNPLs with more MLs, indicating the occurrence of photon-driven transformation during the AI-TA measurement. Compared to photoluminescence, the higher-order peaks are less

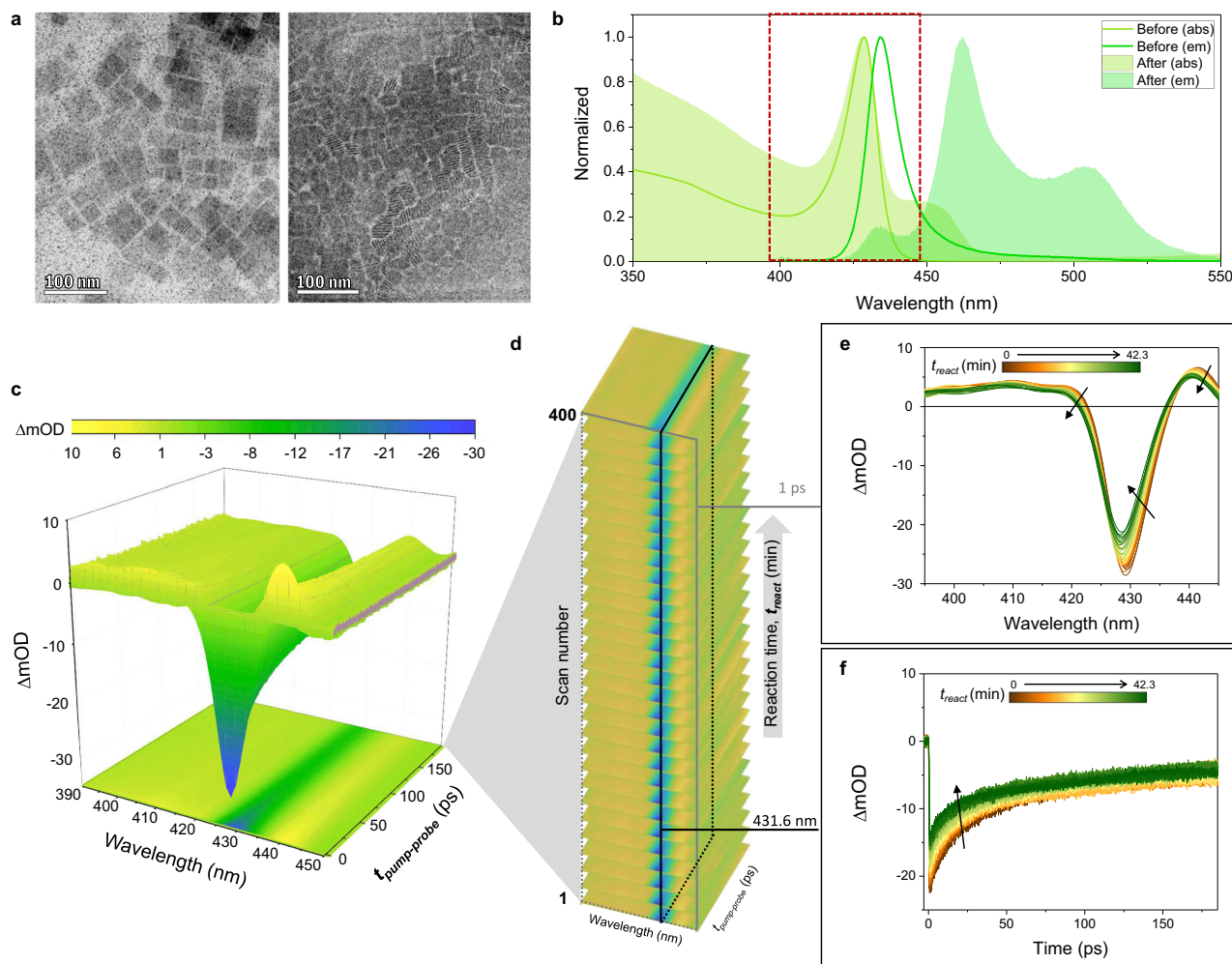
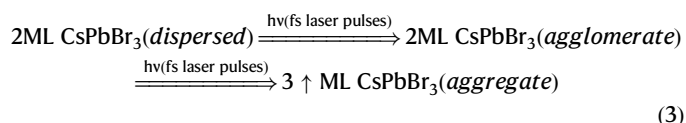


Fig. 5 | In situ and real-time analysis of 2ML PeNPLs kinetics using AI-TA. **a** TEM image of PeNPLs standing face down and side up. The average size in unconfined dimensions is ~20 nm. **b** Normalized absorption and emission spectra of PeNPLs before and after the AI-TA experiment. The probe range is marked with a dotted red square. **c** A transient absorption profile of 2ML PeNPLs acquired by averaging 400

scans of AI-TA. **d** Projection by t_{react} of individual scans participating in the averaged spectrum. **e** A collection of transient spectra at the $t_{\text{pump-probe}}$ of 1 ps for different reaction times. **f** A collection of time profiles at the probe wavelength of 431.6 nm for different reaction times.

prominent in the absorption spectrum because they have higher quantum yields and therefore show stronger photoluminescence^{25,68}. The transformation happening over the course of the experiment, visualized earlier in Fig. 1e, can be summarized with the following Eq. (3).



Another important consideration in this experimental scheme is that the bandgap energies of 3ML and higher-order structures, including bulk material, are much lower and fall outside the spectral range of our near-ultraviolet probe⁶⁸. Therefore, only the first half of the reaction involving only the 2ML PeNPLs and their agglomerate structures is selectively detected. Also note that other perovskite phases, which can form in cesium-poor environments similar to PeNPLs, have higher band gaps and are not considered in this investigation.

Typically, nonlinear responses are small, so transient absorption signals are usually averaged over extended DAQ periods. Here, it

should be emphasized that the effect of sample coalescence is not very evident in the averaged TA measurement of PeNPLs shown in Fig. 5c, which represents the collective response of 400 interferogram scans acquired over ~40 min of t_{react} . However, AI-TA enables us to analyze the data with fewer averages and varying t_{react} durations (Fig. 5d). Unlike traditional TA spectroscopy, we can analyze the spectrum while adjusting the desired measurement time.

By separately analyzing the data in 1-min segments of t_{react} , we observe a blueshift in the transient signals. Additionally, the peak intensity decreases, likely due to sample degradation, as similar trends are observed in the AI-TA scan of PeNCs in toluene (Supplementary Fig. 11), where the intensity diminishes over the course of the scans. Such sample changes would likely interfere with time-profile measurements in conventional systems, where TA spectra are averaged over fixed time intervals.

The complete disappearance of AI-TA signal, marking the complete consumption of 2ML variants, takes longer than 2 h. However, in this study, extended measurements after 400 scans are affected by aggregation at the focus and the formation of higher-order structures, and thus these data are discarded from the analysis (Supplementary Fig. 15). Consequently, this result cannot be directly compared with the post-experiment steady-state spectra. TEM imaging of the measurement sample after collection reveals some mosaic-like structures of

PeNPLs (Supplementary Fig. 16), consistent with previously reported observations.

Spectra of transient signals at a fixed $t_{\text{pump-probe}}$ of 1 ps (Fig. 5e) and a fixed probe wavelength of 431.6 nm (Fig. 5f) were collected to compare the evolution of the signals over reaction time, revealing clear and definite changes. The shifts in the PB signals to lower wavelengths are subtle but noticeable in the AI-TA spectra. The bandgap bleach peak shifts by -1 nm, accompanied by changes in the distribution of excited carrier populations, as indicated by shifts in both sidebands (Supplementary Fig. 17). This effect becomes more pronounced when comparing normalized spectra acquired at different reaction times. This observation can be attributed to the preferential degradation of PeNPLs with larger non-confined dimensions. However, the impact of this parameter on the shift of the excitonic absorption peak is less significant compared to the number of layers, which serves as a more discrete parameter⁶⁸ (Supplementary Fig. 18).

The collection of time profiles at a fixed wavelength (Fig. 5f) shows that the decay trend also changes. The triexponential fit of the time profiles yields three different time constants (Supplementary Fig. 19), which can be interpreted in terms of kinetics similar to those identified earlier in Fig. 2, representing hot carrier thermalization, charge trapping, and carrier recombination⁷⁰.

The shortest component, corresponding to the hot carrier thermalization process, provides a unique insight into the dynamics of PeNPLs. The spectral and temporal signature comprises a sub-picosecond peak redshift, appearing as a decay at shorter wavelengths and as a rise at longer wavelengths. The excess energy of the hot state is lost via electron-phonon coupling. As the measurement progresses, the hot carrier relaxation lifetime of PeNPLs gradually increases from -0.08 to 0.12 ps, indicating a bottleneck in the relaxation dynamics.

Although the hot phonon bottleneck is reported to have a negligible impact on highly confined CsPbBr₃ PeNCs⁷¹, such a slowdown in hot carrier cooling has been observed in superlattice PeNPLs⁷². Similarly, the efficiency of hot phonon cooling is much better in colloidal samples compared to film counterparts with the same number of MLs⁷³. In both cases, carrier cooling has been compared between colloidally dispersed and dried samples and confirmed through power dependence measurements. Another study on a sample aged for 80 days and measured with time-resolved upconversion spectroscopy also reports an increased lifetime³³.

Likewise, our results can be interpreted as an agglomeration-induced suppression of hot carrier relaxation. The excess energy of the hot state is dissipated via electron-phonon coupling to form longitudinal optical phonons^{72,74}. The thermal energy is subsequently transformed into out-of-plane modes and dissipated into the environment, particularly efficiently in highly confined small PeNCs and PeNPLs. However, the formation of stacked structures, known as superlattices, suppresses this out-of-plane coupling and causes a bottleneck in thermal relaxation. In our case, the observation of the hot phonon bottleneck was achieved not by measuring power dependence, but through fast DAQ of the progressing photoinduced agglomeration of PeNPLs.

The other lifetime, associated with the charge-trapping process, remains almost consistent. This lifetime is assumed to be intrinsic to the state of PeNPLs undergoing AI-TA measurement, where femtosecond laser pulses create a photochemically dynamic and highly stressed environment. Another interesting observation is that the lifetimes of the longest component are also increasing. This component reflects exciton recombination, which may involve trapped charges, as observed in the case of PeNCs. This could be related to the size reduction observed alongside the PB peak shift, which involves the removal of incomplete unit cells with vacancies at the edges of the nanoplatelets.

This trend can also be visualized in collections of highly averaged and normalized time profiles at longer wavelengths. One advantage of AI-TA is that it allows control of the length of DAQ for averaging, enabling us to validate the minute changes observed here. Shorter acquisition times result in a lower signal-to-noise ratio, so integrating longer reaction times and analyzing the data over these periods helps clarify the trend observed in the experiment. This is demonstrated by averaging over different reaction times. Comparing the averaged results for 1, 5, and 10 min of t_{react} (Supplementary Fig. 20) confirms the observations made with 1-min averages. Again, we emphasize the strength of the AI-TA technique, particularly its ability to account for changes occurring throughout the measurement process.

Discussion

In this study, we successfully applied the AI-TA technique to the in situ observation of the photophysical behavior of perovskite nanomaterials undergoing photoinduced chemical reactions and transformation processes. We investigated specialized forms of light-induced photodegradation and demonstrated that, in some cases, the measurement process itself can influence the results of a spectroscopic experiment. Our AI-TA technique helps elucidate the impact of such measurement effects. This method offers a streamlined approach for investigating photoinduced dynamic processes across a broad temporal range, from femtoseconds to minutes. By conceptualizing the time taken for the experiment as a chemical reaction axis, this technique can be regarded as an unconventional form of multidimensional spectroscopy. While this experiment focused on perovskite nanomaterials, the methodology holds promise for extension to other photoreactive chemical or biological systems, thereby expanding the scope of its applicability.

In summary, the first study presented here enhances our understanding of the relationship between trap states and chloride-to-bromide variation in CsPb(Br/Cl)₃ PeNCs as a function of reaction time and provides an effective strategy for investigating similar systems. It is worth noting that both experimental verification and theoretical calculations of halide composition variations would typically require substantial resources and time investment. The AI-TA technique effectively addresses these challenges by reducing several months of investigation to just a few minutes, while requiring only a small amount of material for multiple compositions. The second study involving PeNPLs represents an interesting example of bridging photophysical observations between films and colloidal nanoplatelets. This study offers a deeper understanding of the excited-state dynamics and spectral shifts that occur as colloidally dispersed particles aggregate. With the emergence of advanced data handling technologies, where the acquisition of extensive datasets for analysis is crucial, our work stands to make a meaningful contribution to the future of materials research.

Methods

Asynchronous and interferometric transient absorption (AI-TA) spectrometer

The outputs of second-harmonic generation from two Ti:Sapphire mode-locked lasers (Rainbow2, Femtolasers) were used as fundamental light sources, serving as the pump and probe lasers, as well as the radiation sources for photo-substitution reactions of PeNCs. BBO crystals (Cstech) with different critical phase matching conditions were used to convert the laser source wavelength from the near-infrared to the near-ultraviolet region. Their repetition rates were stabilized to 80.0 MHz for the probe and $80.0 \text{ MHz} + \Delta f$ for the pump by phase-locking to an 8-channel frequency synthesizer (HS9008B, Holtzworth) referenced by a GPS-disciplined Rb atomic clock. The detuning frequency, Δf , was set to 51.2 Hz, 153.6 Hz, or

460.8 Hz (8 fs, 24 fs, or 72 fs time steps, respectively) depending on the measurement window of pump-probe time. The digitizer was operated at 80.0 MHz, synchronized with the frequency of the probe pulses, to record light intensity within a preset time interval. The second-harmonic generation signal, produced by the pump and probe overlap on a nonlinear crystal, was used as an optical trigger that established the starting point of decay profiles. Pump and probe pulses were focused using UV-enhanced aluminum off-axis parabolic mirrors at a 1 mm sample cell (21/Q/1, Starna Scientific). The cell contained a sample and was vigorously stirred using a magnetic bar. This stirring serves the dual purpose of minimizing the photo-degradation and the photothermal signals while expediting the equilibrium for anion exchanges, which occur rapidly enough to be considered simultaneous¹⁸. After passing through the sample, the interferogram of the probe pulse was acquired using a balanced photodetector (PDB415A, Thorlabs) in a symmetric configuration⁷⁵. Chirp compensation is performed post-measurement to correct for dispersion at early time delays (<100 fs) (Supplementary Fig. 21). Every experiment was conducted under ambient, room-temperature conditions. MATLAB with embedded function packages was used to analyze data, including the FFT. A more detailed instrumental and theoretical description of the method is provided in Supplementary Notes and Supplementary Fig. 22.

Chemicals

Lead acetate trihydrate ($\text{Pb}(\text{CH}_3\text{COO})_2 \cdot 3\text{H}_2\text{O}$, 99.99%), cesium carbonate (Cs_2CO_3 , reagent Plus, 99%), lead(II) bromide (PbBr_2 , $\geq 98\%$), benzoyl bromide ($\text{C}_6\text{H}_5\text{COBr}$, 97%), benzoyl chloride ($\text{C}_6\text{H}_5\text{COCl}$, 98%), acetone (CH_3COCH_3 , HPLC, $\geq 99.9\%$), toluene (anhydrous, 99.5%), hexane (C_6H_{14} , $\geq 99\%$), chloroform (HPLC Plus, $\geq 99.9\%$), octadecene (ODE, technical grade, 90%), oleylamine (OLAM, 70%), and oleic acid (OA, 90%) were purchased from Sigma-Aldrich. All chemicals were used without any further purification.

Synthesis

CsPbX₃ (X=Cl, Br) perovskite nanocrystals. CsPbX₃ (X=Cl, Br) PeNCs were prepared by following the reported procedure⁷⁶ with slight modifications. In a typical synthesis, cesium carbonate (16 mg), lead acetate trihydrate (76 mg), 0.3 mL of OA, 1 mL of OLAM, and 5 mL of ODE were loaded into a 25 mL 3-neck round-bottom flask and degassed under vacuum for 1 h at 100 °C. Subsequently, the temperature increased to 170 °C under Ar, and 0.6 mmol of the mixture of benzoyl chloride/bromide (a precursor ratio of 1:1) was swiftly injected. The reaction mixture was immediately cooled down in an ice-water bath. Finally, 5 mL of toluene was added to the crude NC solutions, and the resulting mixture was centrifuged for 10 min at 3500 rpm. The supernatant was discarded, and the precipitate was redispersed in 5 mL of toluene for further use.

2ML CsPbBr₃ perovskite nanoplatelets. All-inorganic PeNPLs with the composition CsPbBr₃ were synthesized using a previously reported ligand-assisted reprecipitation method under ambient conditions⁶⁸. Two precursors were prepared prior to conducting the synthesis. One was a solubilized lead bromide (0.01 mmol) in a mixture of 0.1 mL of oleylamine, 0.1 mL of oleic acid, and 10 mL of toluene. The mixture should be stirred and heated at 100 °C until PbBr_2 powder is fully dissolved. The cesium-oleate precursor was prepared by dissolving 0.1 mmol Cs_2CO_3 in 10 mL of oleic acid. This was also stirred and heated at 100 °C until fully dissolved. The ratio of precursors to anti-solvent in the synthesis determines the thickness of the synthesized PeNPLs. In the case of 2ML PeNPLs, 0.15 mL of Cs-oleate precursor was added to a vigorously stirring 3 mL of PbBr_2 precursor. Immediately, 2 mL of acetone serving as an antisolvent was injected, and the mixture was kept stirred for 1 min. Then the solution was transferred to a 50 mL conical tube and centrifuged at 4000 rpm for 3 min. The supernatant

was discarded, and the precipitate was redispersed in 2 mL of hexane. All PeNPL solutions used for AI-TA experiments were kept for no longer than 2 weeks after synthesis.

Steady-state absorption and emission spectroscopy

The absorption and emission spectra of nanocrystals were acquired using Lambda 465 (Perkin Elmer) and Duetta (Horiba), respectively. A quartz cell with a path length of 10 mm was used for the measurement, and the sample was diluted to one-tenth of the stock solution.

X-ray diffraction

A Rigaku D/Max Ultima III X-ray diffractometer with graphite-monochromatized Cu K α ($\lambda = 1.54056 \text{ \AA}$) radiation was used to identify the crystal structure of PeNCs (Supplementary Fig. 23). The PeNC sample solution was drop-casted onto the substrate for measurement. The diffractometer was set to 40 kV with a current of 30 mA, and the spectra were collected from 20° to 60° with a 0.01° sampling width.

X-ray photoelectron spectroscopy

K-alpha (Thermo VG, U.K.) instrument was used to measure the XPS spectra of the PeNCs. The PeNC samples were spin-coated on the silicon substrate for the measurement. The wide scan and narrow scan spectra were obtained by using a monochromatic Al X-ray source (1486.6 eV). The energy step sizes of the survey and narrow scans were 1 eV and 0.1 eV, respectively. The binding energy of the measurement was calibrated by the standard electron energy of 284.8 eV corresponding to the photoelectron from the carbon 1s state.

Transmission electron microscopy

The estimation of PeNC size was performed using a Tecnai G2 F30ST (FEI) microscope. For high-resolution measurement, a 300 S/TEM (Double Cs Corrected Titan3 G2 60, FEI) equipped with ChemiSTEM technology is used.

Time-correlated single-photon counting

TCSPC measurements were conducted using FluoTime300 (Pico-Quant). The sample was excited with a laser with a center wavelength of 405 nm. The photon count data was binned at 25 ps. For the stock sample, PeNC in toluene, and the PeNC sample after the experiment, the detection wavelength was set to 439.8 nm (5 nm bandpass) and 419.8 nm (5 nm bandpass), respectively.

Data availability

All data generated or analyzed during this study are provided in this article and its supplementary information. Source data are provided with this paper.

References

1. Elzinga, P. A. et al. Pump/probe method for fast analysis of visible spectral signatures utilizing asynchronous optical sampling. *Appl. Opt.* **26**, 4303 (1987).
2. Bartels, A. et al. Ultrafast time-domain spectroscopy based on high-speed asynchronous optical sampling. *Rev. Sci. Instrum.* **78**, 035107 (2007).
3. Kim, J., Yoon, T. H. & Cho, M. Interferometric measurement of transient absorption and refraction spectra with dual frequency comb. *J. Phys. Chem. B* **122**, 9775–9785 (2018).
4. Han, N. S., Kim, J., Yoon, T. H. & Cho, M. Time-resolved spectroscopy of thioflavin T solutions: asynchronous optical sampling method with two frequency-upconverted mode-locked lasers. *J. Chem. Phys.* **156**, 064201 (2022).
5. Kim, J., Jeon, J., Yoon, T. H. & Cho, M. Two-dimensional electronic spectroscopy of bacteriochlorophyll a with synchronized dual mode-locked lasers. *Nat. Commun.* **11**, 6029 (2020).

6. Kim, J. et al. Low-frequency vibronic mixing modulates the excitation energy flow in bacterial light-harvesting complex II. *J. Phys. Chem. Lett.* **12**, 6292–6298 (2021).
7. Han, G. R., Jang, H., Yoon, T. H. & Cho, M. Asynchronous and interferometric nonlinear spectroscopy (AI-NS): expanding temporal and spectral horizons. *J. Phys. Chem. B* **129**, 1891–1903 (2025).
8. Zhang, F. et al. Brightly luminescent and color-tunable colloidal $\text{CH}_3\text{NH}_3\text{PbX}_3$ (X = Br, I, Cl) quantum dots: potential alternatives for display technology. *ACS Nano* **9**, 4533–4542 (2015).
9. Rainò, G. et al. Single cesium lead halide perovskite nanocrystals at low temperature: fast single-photon emission, reduced blinking, and exciton fine structure. *ACS Nano* **10**, 2485–2490 (2016).
10. Nenon, D. P. et al. Design principles for trap-free CsPbX_3 nanocrystals: enumerating and eliminating surface halide vacancies with softer Lewis bases. *J. Am. Chem. Soc.* **140**, 17760–17772 (2018).
11. Hintermayr, V. A. et al. Tuning the optical properties of perovskite nanoplatelets through composition and thickness by ligand-assisted exfoliation. *Adv. Mater.* **28**, 9478–9485 (2016).
12. Kovalenko, M. V., Protesescu, L. & Bodnarchuk, M. I. Properties and potential optoelectronic applications of lead halide perovskite nanocrystals. *Science* **358**, 745–750 (2017).
13. Protesescu, L. et al. Nanocrystals of cesium lead halide perovskites (CsPbX_3 , X = Cl, Br, and I): novel optoelectronic materials showing bright emission with wide color gamut. *Nano Lett.* **15**, 3692–3696 (2015).
14. Wang, L. et al. Scalable ligand-mediated transport synthesis of organic–inorganic hybrid perovskite nanocrystals with resolved electronic structure and ultrafast dynamics. *ACS Nano* **11**, 2689–2696 (2017).
15. Becker, M. A. et al. Bright triplet excitons in caesium lead halide perovskites. *Nature* **553**, 189–193 (2018).
16. Swarnkar, A. et al. Colloidal CsPbBr_3 perovskite nanocrystals: luminescence beyond traditional quantum dots. *Angew. Chem. Int. Ed.* **54**, 15424–15428 (2015).
17. An, M. N. et al. Low-temperature molten salts synthesis: CsPbBr_3 nanocrystals with high photoluminescence emission buried in mesoporous SiO_2 . *ACS Energy Lett.* **6**, 900–907 (2021).
18. Nedelcu, G. et al. Fast anion-exchange in highly luminescent nanocrystals of cesium lead halide perovskites (CsPbX_3 , X = Cl, Br, I). *Nano Lett.* **15**, 5635–5640 (2015).
19. Parobek, D., Dong, Y., Qiao, T., Rossi, D. & Son, D. H. Photoinduced anion exchange in cesium lead halide perovskite nanocrystals. *J. Am. Chem. Soc.* **139**, 4358–4361 (2017).
20. Wong, Y. et al. Color patterning of luminescent perovskites via light-mediated halide exchange with haloalkanes. *Adv. Mater.* **31**, 1901247 (2019).
21. Sandeep, K. et al. Overcoming the photoinduced solvent-assisted anion exchange reactions of CsPbBr_3 perovskite nanocrystals. *J. Phys. Chem. C* **127**, 14495–14501 (2023).
22. Zhao, L., Yin, C., Long, T., Hu, P. & Yang, Z. Light-driven halide exchange facilitates complete crystal transformation in nanostructured perovskites. *Langmuir* **36**, 3064–3071 (2020).
23. Kubo, N., Yamauchi, M. & Masuo, S. Solvent dependence of the photoinduced anion exchange reaction of cesium lead halide perovskite nanocrystals. *Chem. Lett.* **50**, 1483–1485 (2021).
24. Qiao, T., Parobek, D., Dong, Y., Ha, E. & Son, D. H. Photoinduced Mn doping in cesium lead halide perovskite nanocrystals. *Nanoscale* **11**, 5247–5253 (2019).
25. Weidman, M. C., Seitz, M., Stranks, S. D. & Tisdale, W. A. Highly tunable colloidal perovskite nanoplatelets through variable cation, metal, and halide composition. *ACS Nano* **10**, 7830–7839 (2016).
26. Dang, Z. et al. Temperature driven transformation of CsPbBr_3 nanoplatelets into mosaic nanotiles in solution through self-assembly. *Nano Lett.* **20**, 1808–1818 (2020).
27. Prabhakaran, A. et al. Real-time in situ observation of CsPbBr_3 perovskite nanoplatelets transforming into nanosheets. *ACS Nano* **17**, 13648–13658 (2023).
28. Wang, Y. et al. Photon driven transformation of cesium lead halide perovskites from few-monolayer nanoplatelets to bulk phase. *Adv. Mater.* **28**, 10637–10643 (2016).
29. Roy, M., Vikram, Bhawna, Alam, A. & Aslam, M. Photoinduced quasi-2D to 3D phase transformation in hybrid halide perovskite nanoplatelets. *Phys. Chem. Chem. Phys.* **23**, 27355–27364 (2021).
30. Zhang, H. et al. Light-induced transformation of all-inorganic mixed-halide perovskite nanoplatelets: ion migration and coalescence. *Opt. Express* **32**, 22340 (2024).
31. Shamsi, J. et al. Bright-emitting perovskite films by large-scale synthesis and photoinduced solid-state transformation of CsPbBr_3 nanoplatelets. *ACS Nano* **11**, 10206–10213 (2017).
32. DuBose, J. T., Christy, A., Chakkamalayath, J. & Kamat, P. V. Transformation of perovskite nanoplatelets to large nanostructures driven by solvent polarity. *ACS Mater. Lett.* **4**, 93–101 (2022).
33. Socie, E., Vale, B. R. C., Burgos-Caminal, A. & Moser, J. Direct observation of shallow trap states in thermal equilibrium with band-edge excitons in strongly confined CsPbBr_3 perovskite nanoplatelets. *Adv. Opt. Mater.* **9**, 2001308 (2021).
34. Jana, A. et al. Self-assembly of perovskite nanocrystals. *Prog. Mater. Sci.* **129**, 100975 (2022).
35. Kobayashi, M. et al. High-acquisition-rate single-shot pump-probe measurements using time-stretching method. *Sci. Rep.* **6**, 37614 (2016).
36. Adhikari, S. et al. Accelerating ultrafast spectroscopy with compressive sensing. *Phys. Rev. Appl.* **15**, 024032 (2021).
37. Picqué, N. & Hänsch, T. W. Frequency comb spectroscopy. *Nat. Photonics* **13**, 146–157 (2019).
38. Cho, B., Yoon, T. H. & Cho, M. Dual-comb spectroscopy of molecular electronic transitions in condensed phases. *Phys. Rev. A* **97**, 033831 (2018).
39. Jang, H. et al. Unveiling ultrafast carrier dynamics of tellurium microcrystals by two-color asynchronous sampling infrared transient absorption spectroscopy. *J. Phys. Chem. C* **128**, 268–278 (2024).
40. Ashner, M. N. et al. Size-dependent biexciton spectrum in CsPbBr_3 perovskite nanocrystals. *ACS Energy Lett.* **4**, 2639–2645 (2019).
41. Butkus, J. et al. The evolution of quantum confinement in CsPbBr_3 perovskite nanocrystals. *Chem. Mater.* **29**, 3644–3652 (2017).
42. Qiao, T. & Son, D. H. Synthesis and properties of strongly quantum-confined cesium lead halide perovskite nanocrystals. *Acc. Chem. Res.* **54**, 1399–1408 (2021).
43. Knezevic, M. et al. Adjusting the band gap of $\text{CsPbBr}_{3-y}\text{X}_y$ (X = Cl, I) for optimal interfacial charge transfer and enhanced photocatalytic hydrogen generation. *J. Mater. Chem. A* **11**, 6226–6236 (2023).
44. Shen, X. et al. Red shift of bleaching signals in femtosecond transient absorption spectra of CsPbX_3 (X = Cl/Br, Br, Br/I) nanocrystals induced by the biexciton effect. *J. Phys. Chem. C* **125**, 5278–5287 (2021).
45. Fu, J. et al. Hot carrier cooling mechanisms in halide perovskites. *Nat. Commun.* **8**, 1300 (2017).
46. Yarita, N. et al. Dynamics of charged excitons and biexcitons in CsPbBr_3 perovskite nanocrystals revealed by femtosecond transient-absorption and single-dot luminescence spectroscopy. *J. Phys. Chem. Lett.* **8**, 1413–1418 (2017).

47. Soetan, N. et al. Ultrafast spectral dynamics of CsPb(Br_xCl_{1-x})₃ mixed-halide nanocrystals. *ACS Photonics* **5**, 3575–3583 (2018).
48. Mondal, N. & Samanta, A. Complete ultrafast charge carrier dynamics in photo-excited all-inorganic perovskite nanocrystals (CsPbX₃). *Nanoscale* **9**, 1878–1885 (2017).
49. Lai, R. & Wu, K. Picosecond electron trapping limits the emissivity of CsPbCl₃ perovskite nanocrystals. *J. Chem. Phys.* **151**, 194701 (2019).
50. Malý, P. et al. Separating single- from multi-particle dynamics in nonlinear spectroscopy. *Nature* **616**, 280–287 (2023).
51. Luo, C. et al. Ultrafast thermodynamic control for stable and efficient mixed halide perovskite nanocrystals. *Adv. Funct. Mater.* **30**, 2000026 (2020).
52. Nakahara, S. et al. Suppression of trion formation in CsPbBr₃ perovskite nanocrystals by postsynthetic surface modification. *J. Phys. Chem. C* **122**, 22188–22193 (2018).
53. Lorenc, M. et al. Artifacts in femtosecond transient absorption spectroscopy. *Appl. Phys. B Lasers Opt.* **74**, 19–27 (2002).
54. Mandal, S. et al. Unravelling halide-dependent charge carrier dynamics in CsPb(Br/Cl)₃ perovskite nanocrystals. *Nanoscale* **13**, 3654–3661 (2021).
55. Chung, H. et al. Composition-dependent hot carrier relaxation dynamics in cesium lead halide (CsPbX₃, X=Br and I) perovskite nanocrystals. *Angew. Chem.* **129**, 4224–4228 (2017).
56. Kolda, T. G. & Bader, B. W. Tensor decompositions and applications. *SIAM Rev.* **51**, 455–500 (2009).
57. TP Tool. MATLAB Central File Exchange. <https://www.mathworks.com/matlabcentral/fileexchange/25514-tp-tool> (2023).
58. Saliba, M. et al. Cesium-containing triple cation perovskite solar cells: improved stability, reproducibility and high efficiency. *Energy Environ. Sci.* **9**, 1989–1997 (2016).
59. Jeon, N. J. et al. Compositional engineering of perovskite materials for high-performance solar cells. *Nature* **517**, 476–480 (2015).
60. Prakash, J. et al. Progress in tailoring perovskite based solar cells through compositional engineering: Materials properties, photovoltaic performance and critical issues. *Mater. Today Energy* **9**, 440–486 (2018).
61. Tian, J. et al. Composition engineering of all-inorganic perovskite film for efficient and operationally stable solar cells. *Adv. Funct. Mater.* **30**, 2001764 (2020).
62. Tong, Y. et al. In situ halide exchange of cesium lead halide perovskites for blue light-emitting diodes. *Adv. Mater.* **35**, 2207111 (2023).
63. Zhu, C. et al. Room-temperature, highly pure single-photon sources from all-inorganic lead halide perovskite quantum dots. *Nano Lett.* **22**, 3751–3760 (2022).
64. Qaid, S. M. H., Ghaitan, H. M., Al-Asbahi, B. A. & Aldwayyan, A. S. Tuning of amplified spontaneous emission wavelength for green and blue light emission through the tunable composition of CsPb(Br_{1-x}Cl_x)₃ inorganic perovskite quantum dots. *J. Phys. Chem. C* **125**, 9441–9452 (2021).
65. Jacobsson, T. J. et al. An open-access database and analysis tool for perovskite solar cells based on the FAIR data principles. *Nat. Energy* **7**, 107–115 (2021).
66. Lignos, I., Maceiczky, R. M., Kovalenko, M. V. & Stavrakis, S. Tracking the fluorescence lifetimes of cesium lead halide perovskite nanocrystals during their synthesis using a fully automated optofluidic platform. *Chem. Mater.* **32**, 27–37 (2020).
67. Wu, Y. et al. Amine-free CsPbBr₃ perovskite nanoplatelets produced with monolayer-precision thickness control. *ACS Mater. Lett.* **6**, 2425–2433 (2024).
68. Bohn, B. J. et al. Boosting tunable blue luminescence of halide perovskite nanoplatelets through postsynthetic surface trap repair. *Nano Lett.* **18**, 5231–5238 (2018).
69. Carwithen, B. P. et al. Confinement and exciton binding energy effects on hot carrier cooling in lead halide perovskite nanomaterials. *ACS Nano* **17**, 6638–6648 (2023).
70. Marjit, K. et al. Structural analysis and carrier relaxation dynamics of 2D CsPbBr₃ nanoplatelets. *J. Phys. Chem. C* **125**, 12214–12223 (2021).
71. Li, Y. et al. On the absence of a phonon bottleneck in strongly confined CsPbBr₃ perovskite nanocrystals. *Chem. Sci.* **10**, 5983–5989 (2019).
72. Sun, Q. et al. Elucidating the unique hot carrier cooling in two-dimensional inorganic halide perovskites: the role of out-of-plane carrier–phonon coupling. *Nano Lett.* **22**, 2995–3002 (2022).
73. Villamil Franco, C. et al. Exciton cooling in 2D perovskite nanoplatelets: rationalized carrier-induced Stark and phonon bottleneck effects. *J. Phys. Chem. Lett.* **13**, 393–399 (2022).
74. Wang, Y. et al. Strong triplet-exciton–LO-phonon coupling in two-dimensional layered organic–inorganic hybrid perovskite single crystal microflakes. *J. Phys. Chem. Lett.* **12**, 2133–2141 (2021).
75. Coddington, I., Newbury, N. & Swann, W. Dual-comb spectroscopy. *Optica* **3**, 414 (2016).
76. Imran, M. et al. Benzoyl halides as alternative precursors for the colloidal synthesis of lead-based halide perovskite nanocrystals. *J. Am. Chem. Soc.* **140**, 2656–2664 (2018).

Acknowledgements

This work was supported by the Institute for Basic Science (IBS-RO23-D1) for M.C. and NRF-2022M3K4A1094781 for T.H.Y. We wish to thank K.J. Lee and J.M. Lim for their discussion and comments on the project, B.G. Choi for the assistance with the debugging of scripts, D.W. Jeong for insightful comments on materials analysis, W.J. Cho for advice on the synthesis protocol, and RIAM (Research Institute of Advanced Materials, Seoul National University) for TCSPC measurement.

Author contributions

Conceptualization: G.R.H., T.H.Y., M.C.; funding acquisition: M.C.; investigation: G.R.H.—AI-TA/UV-VIS/PL/TCSPC, M.N.A.—XRD/XPS/TEM; methodology: G.R.H., T.H.Y., M.C.; project administration: G.R.H., T.H.Y., M.C.; resources: M.N.A., G.R.H., K.S.J.—materials, N.S.H., J.W.K., G.R.H.—instrumentation; software: J.W.K., G.R.H., H.J.; supervision: T.H.Y., M.C.; validation: G.R.H., T.H.Y., H.J., M.C.; visualization: G.R.H., T.H.Y., M.C.; writing—original draft: G.R.H.; writing—review & editing: all authors.

Competing interests

The authors declare no competing interests.

Additional information

Supplementary information The online version contains supplementary material available at <https://doi.org/10.1038/s41467-025-60313-3>.

Correspondence and requests for materials should be addressed to Tai Hyun Yoon or Minhaeng Cho.

Peer review information *Nature Communications* thanks the anonymous reviewer(s) for their contribution to the peer review of this work. A peer review file is available.

Reprints and permissions information is available at <http://www.nature.com/reprints>

Publisher's note Springer Nature remains neutral with regard to jurisdictional claims in published maps and institutional affiliations.

Open Access This article is licensed under a Creative Commons Attribution-NonCommercial-NoDerivatives 4.0 International License, which permits any non-commercial use, sharing, distribution and reproduction in any medium or format, as long as you give appropriate credit to the original author(s) and the source, provide a link to the Creative Commons licence, and indicate if you modified the licensed material. You do not have permission under this licence to share adapted material derived from this article or parts of it. The images or other third party material in this article are included in the article's Creative Commons licence, unless indicated otherwise in a credit line to the material. If material is not included in the article's Creative Commons licence and your intended use is not permitted by statutory regulation or exceeds the permitted use, you will need to obtain permission directly from the copyright holder. To view a copy of this licence, visit <http://creativecommons.org/licenses/by-nc-nd/4.0/>.

© The Author(s) 2025